ACS MATERIALS Au
AN OPEN ACCESS JOURNAL OF THE AMERICAN CHEMICAL SOCIETY

pubs.acs.org/materialsau
Article

Tunable Photocatalytic Activity of CoFe Prussian Blue Analogue Modified $SrTiO_3$ Core–Shell Structures for Solar-Driven Water Oxidation

Naeimeh Sadat Peighambardoust, Sina Sadigh Akbari, Rana Lomlu, Umut Aydemir,* and Ferdi Karadas*

Cite This: *ACS Mater. Au* 2024, 4, 214–223
Read Online

ABSTRACT: This study presents a pioneering semiconductor-catalyst core–shell architecture designed to enhance photocatalytic water oxidation activity significantly. This innovative assembly involves the in situ deposition of CoFe Prussian blue analogue (PBA) particles onto $SrTiO_3$ (STO) and blue $SrTiO_3$ (bSTO) nanocubes, effectively establishing a robust p–n junction, as demonstrated by Mott–Schottky analysis. Of notable significance, the STO/PB core–shell catalyst displayed remarkable photocatalytic performance, achieving an oxygen evolution rate of 129.6 μmol g^{-1} h^{-1}, with stability over an extended 9-h in the presence of $S_2O_8^{2-}$ as an electron scavenger. Thorough characterization unequivocally verified the precise alignment of the band energies within the STO/PB core–shell assembly. Our research underscores the critical role of tailored semiconductor-catalyst interfaces in advancing the realm of photocatalysis and its broader applications in renewable energy technologies.

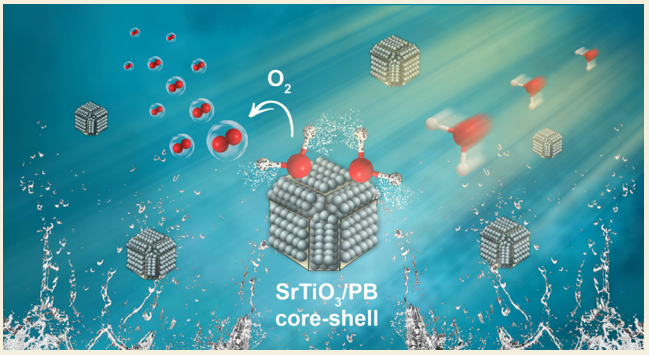

KEYWORDS: *photocatalytic water oxidation, core–shell structure, strontium titanate, Co–Fe Prussian blue analogue, p–n junction*

1. INTRODUCTION

Sunlight is the most plentiful and promising renewable energy source for addressing the world's energy demands. Photocatalytic water splitting with a particulate semiconductor without an external bias has attracted much attention since it offers a simple, cost-effective, and easily scalable strategy for solar light harvesting.[1−3] Perovskite-type strontium titanate ($SrTiO_3$) is one of the most widely investigated oxide-based semiconductors for water splitting due to its proper band structure, low cost, and photochemical stability.[4,5] However, the wide band gap of $SrTiO_3$ (3.2 eV) limits the light response efficiency, and the rapid recombination rate of photogenerated charge carriers results in poor photocatalytic water splitting efficiency of $SrTiO_3$.[6,7] Thus, several modification strategies have been proposed to broaden the spectral response range of $SrTiO_3$ and prevent the photogenerated electron–hole recombination such as metal element doping, creating oxygen vacancies, and cocatalyst deposition.[6−12]

Oxygen defects are being explored to enhance semiconductor photocatalysis.[13,14] While bulk oxygen defects only serve as charge carrier traps where photoinduced electron–hole pairs recombine, surface oxygen vacancies act as the charge traps and the adsorption sites, in which the charge can transfer to the adsorbed species, thereby effectively inhibiting the recombination of photogenerated charge carriers.[15,16] Adjusting the bulk-to-surface defect ratio in TiO_2 nanocrystals improves electron–hole separation and photocatalytic activity.[17] Modifying surface oxygen vacancies in $SrTiO_3$ holds promise for better photocatalytic water splitting. Sun et al.[18] hydrogenated $SrTiO_3$ to enhance charge separation, while Tan et al.[19] created surface oxygen vacancies using a solid-state reaction of $NaBH_4$, yielding various $SrTiO_3$ types with differing vacancy concentrations.

Coupling with a cocatalyst could also improve the photocatalytic activity of a semiconductor catalyst by facilitating charge separation and transfer, suppressing the recombination reaction of photogenerated electron–hole pairs, and accelerating the rate of water splitting redox reactions. Various metals and their oxides have been combined with $SrTiO_3$ as cocatalysts; however, some of these compounds include precious elements that make them impractical for widespread utilization.[20−25] As a result, developing catalytic assemblies based on earth-abundant metals could lead to the advancement of low-cost and noble-metal-free systems for water splitting. CoFe Prussian blue analogues (PBAs) are coordination polymers with a general

Received: October 20, 2023
Revised: November 21, 2023
Accepted: November 28, 2023
Published: December 18, 2023

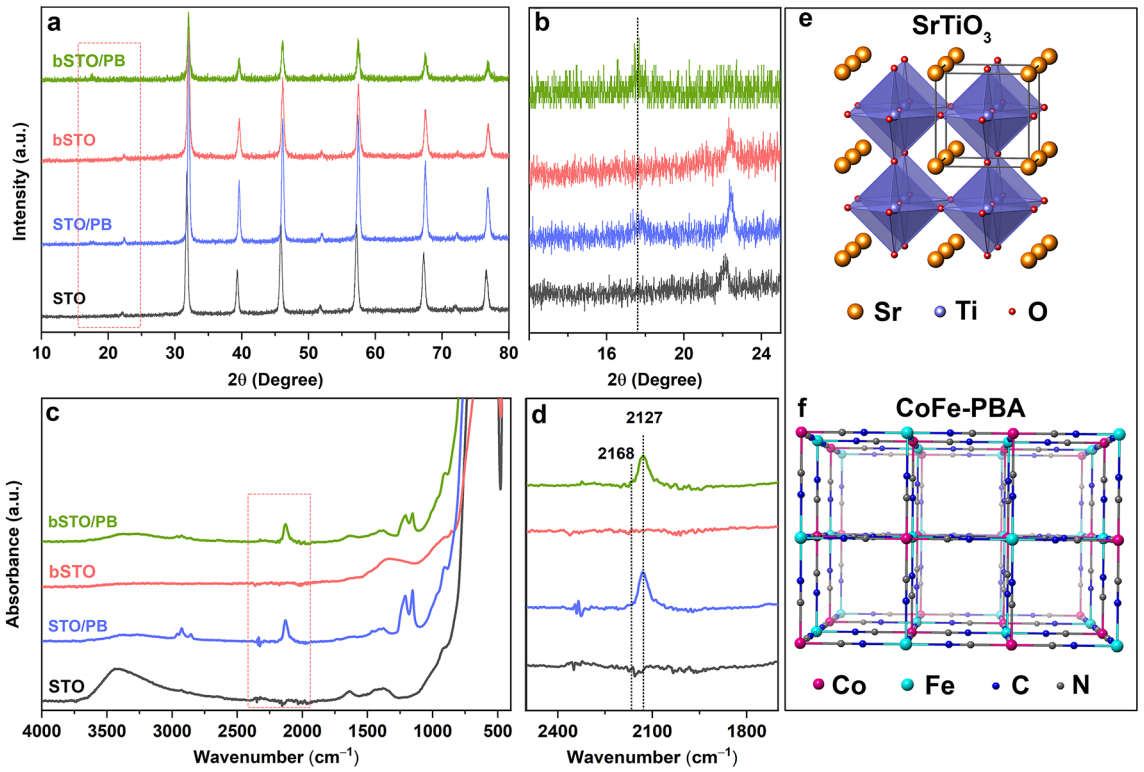

Figure 1. (a,b) XRD patterns of STO, bSTO, STO/PB, and bSTO/PB samples. (c) ATR−FTIR spectra of STO, bSTO, STO/PB, and bSTO/PB samples. (d) Cyanide stretching mode. Crystal structures of (e) $SrTiO_3$ and (f) CoFe-PBA.

formula of $A_xCo_y[Fe(CN)_6].nH_2O$ (where A is an alkali or an alkaline earth metal ion occupying the tetrahedral interstitial sites), which consist of metal ions connected through cyanide bridging ligand.[26] They have recently been acknowledged as water oxidation catalysts due to their simple synthetic protocols, high stabilities, and fast electron transfer between metal ions.[27−31] In a Co−Fe PBA, cobalt sites coordinated to at least one water molecule are active catalytic sites, while the iron sites are catalytically inactive due to the lack of an available coordination site for catalytic reactions.[32,33] Given the poor photoresponse of CoFe-PBAs, the general strategy to develop a PB-based photocatalytic assembly is to combine CoFe-PBAs with a proper photosensitizer and/or a semiconductor.[34−36] The energy level match between the valence band (VB) of the semiconductor and the highest occupied molecular orbital (HOMO) of the catalyst plays a critical role in the water oxidation performance of PB-based assemblies. Our group has developed several hybrid assemblies in which CoFe−PBA as the water oxidation catalyst is coupled with various oxide-based semiconductors, such as niobate nanosheets,[37] brown-TiO_2,[38] and $BiVO_4$[39,40] for light-driven water oxidation.

Building on the projected energy levels of $SrTiO_3$ and drawing inspiration from surface oxygen vacancies found in reduced $SrTiO_3$, known as "blue $SrTiO_3$", herein we combined these materials with Co−Fe PBAs utilizing a pioneering in situ coating approach. The outcome is the creation of PB-coated $SrTiO_3$ nanoparticles, which, in turn, amplifies the water oxidation performance within the ensuing core−shell design. In this study, we have developed a novel semiconductor-catalyst core−shell structure aimed at significantly improving the efficiency of photocatalytic water oxidation. This inventive assembly entails the application of CoFe PBA particles onto nanocubes made of STO and bSTO. This process establishes a sturdy p−n junction, conclusively demonstrated through Mott−Schottky analysis. Remarkably, the STO/PB core−shell catalyst exhibits exceptional photocatalytic performance, achieving an impressive reaction rate of 129.6 μmol g^{-1} h^{-1} while maintaining stability over an extended 9-h period, especially when utilizing S_2O8_2 as an electron scavenger.

2. RESULTS AND DISCUSSION

2.1. Chemical Studies

STO and bSTO were synthesized according to the procedures reported in the literature.[19] The STO and bSTO nanoparticles were mixed with a $[Fe(CN)_6]^{3-}$ solution and subsequently reacted with cobalt ions to afford a hybrid assembly (abbreviated as STO/PB and bSTO/PB). The in situ coating method yields a core−shell structure consisting of $SrTiO_3$ nanoparticles coated with a uniform PB layer. Figure 1a shows the XRD patterns of the pristine STO and bSTO, as well as hybrid assemblies. The STO and bSTO XRD patterns exhibit no impurity phase, confirming that the $SrTiO_3$ structures were successfully prepared. The presence of a broad peak at 2θ = 17.5°, along with low intensity, confirms the production of a thin layer of PB on both STO and bSTO particles (Figure 1b).[28,37] The characteristic Ti−O band was observed at 534 and 542 cm^{-1} in the STO and bSTO FTIR spectra, respectively. However, this band displays a shift to higher wavenumbers for the STO/PB (541 cm^{-1}) and bSTO/PB (544 cm^{-1}). The IR spectra of hybrid assemblies exhibit a strong band at 2127 cm^{-1} and a shoulder at 2168 cm^{-1}, which are attributed to Co(III)−NC−Fe(II) and Co(II)−NC−Fe(III) coordination modes of cyanide in CoFe-PB structure, respectively.[41,42] The broad band at ca. 3386 cm^{-1} is attributed to the OH stretching mode of water molecules on the surface of the particles and in the interstitial lattice of the

https://doi.org/10.1021/acsmaterialsau.3c00090
ACS Mater. Au 2024, 4, 214−223

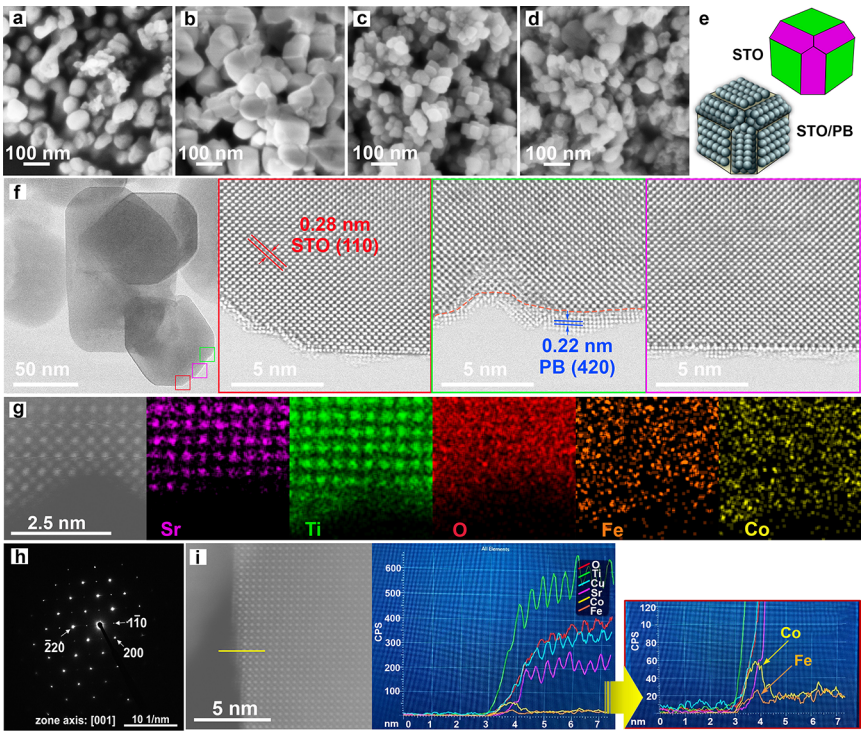

Figure 2. Morphological, structural, and microstructural characterizations of the samples. (a−d) FESEM images of STO, bSTO, STO/PB, and bSTO/PB, respectively. (e) Schematic of STO and STO/PB multifacet crystal shape, (f) HR−TEM images related to STO/PB, red, green, and magenta squares showing the HR-TEM images of core−shell, (g) HAADF−STEM image and the corresponding EDS−STEM mappings of STO/PB, (h) SAED pattern of STO/PB, and (i) EDS line scans of STO/PB core−shell.

framework (Figure 1c,d). The crystal structures of $SrTiO_3$ and CoFe-PBA are shown in Figure 1e and f, respectively.

The morphology of the catalysts was analyzed using FESEM. The SEM images of STO, bSTO, STO/PB, and bSTO/PB are presented in Figure 2a−d and Figure S1. From the images, it can be inferred that the nanoparticles have a nearly spherical shape with anisotropic facets and an average diameter of approximately 50 nm. Moreover, no significant changes were observed among the different samples, except for the average diameter of the bSTO nanoparticle, which increased to approximately 100 nm with an anisotropic facet structure that remained intact. Figure 2e illustrates a schematic representation of the anisotropic facets of the shape of the STO nanoparticle's shape. The surface atomic configuration and coordination of photocatalysts play a crucial role in determining their efficiency for photocatalytic applications. It is widely acknowledged that the different exposed facets of crystals can display exclusive electronic and optical properties and exhibit diverse adsorption properties for ions/molecules.[4]

To further interpret the crystal structure and morphology of the as-obtained catalysts, HR-TEM, SAED, HAADF−STEM, and EDS−STEM were utilized. The TEM image of STO/PB, presented in Figure 2f, illustrates the anisotropic facets of the nanoparticles. The HRTEM photographs exhibit a lattice spacing of 0.28 nm (red square), which can be well indexed to (110) planes of the cubic perovskite structure of $SrTiO_3$ with a $Pm\bar{3}m$ pace group. As evidenced by the literature,[4] the {110} facet of $SrTiO_3$ crystal can be terminated with SrTiO, and this particular facet exhibits a longer bulk carrier lifetime. The third image from left to right (green square) reveals the PB shell lattice fringes with an interplanar distance of 0.22 nm, which can be assigned to (420) planes of a face-centered cubic CoFe Prussian blue structure with a $Fm\bar{3}m$ space group. The red, green, and magenta squares virtualize the HRTEM images of the core−shell structure of STO/PB at different points of the core−shell structure. As depicted in the images, the STO core is surrounded by a PB shell consisting of a few atomic layers. Furthermore, the PB exhibits a preference for binding to certain facets of the crystal, leading to a facet-specific assembly. Based on the visual analysis of the images, it can be inferred that the PB cocatalyst is predominantly loaded on the side facets of the STO crystal (red and green squares). In contrast, the middle facet of the STO crystal appears to have a thinner layer of PB cocatalyst, consisting of only one or two atomic layers (magenta square). This observation suggests that the surface properties and electronic structure of different STO crystal facets can influence the deposition and distribution of the cocatalyst, leading to a facet-specific assembly. It should be highlighted that the HRTEM image of bSTO/PB also exhibits a core−shell structure with an interplanar distance of 0.39 nm for the $SrTiO_3$ core (indexed to (100) planes) and 0.22 nm for the PB shell (assigned to (420) planes of FCC of CoFe Prussian blue; see Figure S2).

The HAADF−STEM image shown in Figure 2g for the STO/PB sample indicates that the Sr, Ti, O, Fe, and Co elements are evenly distributed on the nanoparticle surface. Figure 2h illustrates the SAED patterns of STO/PB along the zone axis [001], verifying the formation of the cubic perovskite structure of $SrTiO_3$. To further broaden our knowledge on verifying the PB shell, EDS line scans of the STO/PB core−shell were performed, as shown in Figure 2i. The resulting line scan graph clearly indicates the presence of Fe and Co elements.

To verify the chemical valences and constituents of the as-prepared catalysts, XPS was utilized, and the outcomes are

https://doi.org/10.1021/acsmaterialsau.3c00090
ACS Mater. Au 2024, 4, 214−223

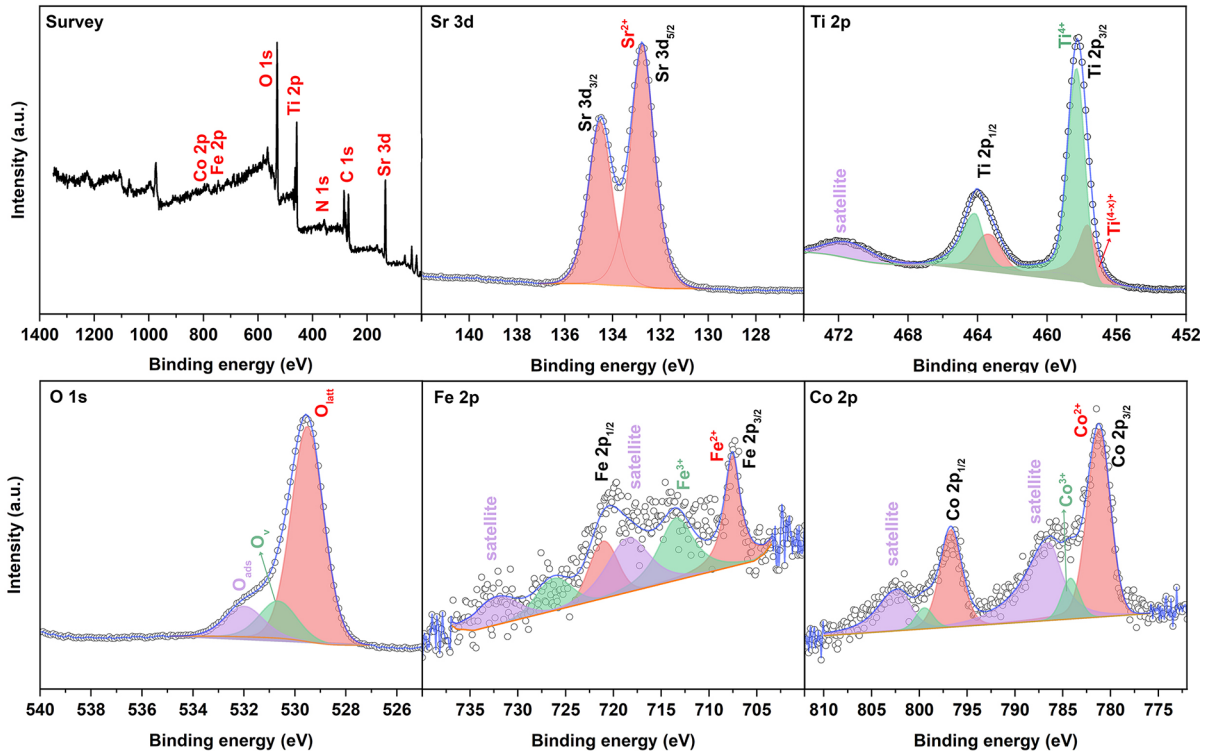

Figure 3. High-resolution XPS spectra of Sr 3d, Ti 2p, O 1s, Co 2p, and Fe 2p for the STO/PB catalyst.

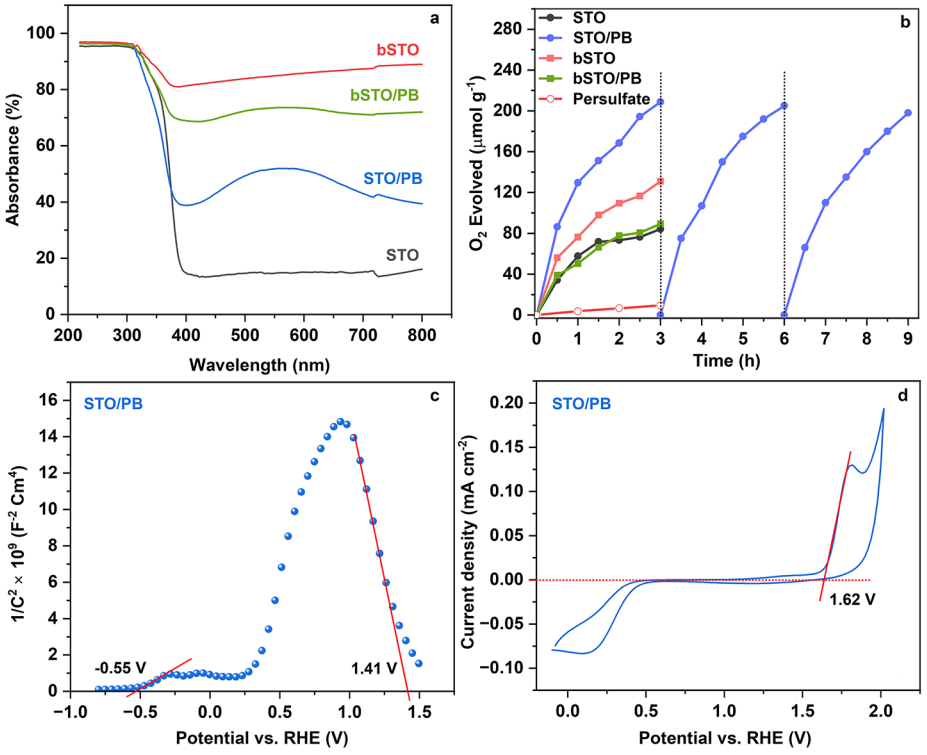

Figure 4. (a) Diffuse reflectance UV−vis spectra of STO, bSTO, STO/PB, and bSTO/PB catalysts. (b) Photocatalytic oxygen evolution activities of STO, bSTO, STO/PB, and bSTO/PB (μmol of generated O_2/g of catalyst) in water containing 5 mg of the catalyst and 5 mM $Na_2S_2O_8$ as the sacrificial agent under UV−vis irradiation (300 W Xe lamp). (c,d) Mott−Schottky and CV plots of STO/PB sample in 0.5 M Na_2SO_4 electrolyte (pH = 7.05) at a scan rate of 50 mV/s.

depicted in Figure 3 and Figure S3. Figure 3 reveals high-resolution XPS spectra of Sr 3d, Ti 2p, O 1s, Co 2p, and Fe 2p for the STO/PB powder. As shown in Figure 3, Sr 3d spectrum displays one doublet at binding energy (BEs), 132.76 and 134.51 eV. According to the literature, the pair belongs to Sr^{2+}, ascribed to the SrO crystal phase.[43] The deconvolution of the Ti 2p spectrum for STO/PB revealed the presence of two sets of doublets, one at lower BEs 457.68, 463.41 eV and the other pair

https://doi.org/10.1021/acsmaterialsau.3c00090
ACS Mater. Au 2024, 4, 214−223

at higher BEs, 458.29, 464.19 eV along with their respective satellite. It is well-known that the former pair belongs to the Ti^{4+} oxidation states in $SrTiO_3$. Nonetheless, the latter doublet indicates the presence of titanium in a low valence state, which might be Ti^{3+} or Ti^{2+}, in the nonstoichiometric $SrTiO_{3-x}$ species.[44] This observation suggests that oxygen vacancies are present in the surface layer of $SrTiO_3$, leading to the reduction of Ti species. Moreover, the initial indication suggests that the surface of the STO/PB sample primarily consists of SrO and TiO species layers, which are believed to possess enhanced water adsorption and dissociation capabilities. This finding also aligns with the deconvolution results obtained from the O 1s spectra of STO/PB. Based on the analysis of the O 1s spectra of STO/PB, three distinct peaks at BEs of around 529.44, 530.21, and 531.59 eV were attributed to metal−oxygen bonding or lattice oxygen (O_{latt}), oxygen vacancy (O_v), and adsorbed hydroxyl groups (O_{ads}) on the surface.

Finally, the Fe 2p spectrum exhibits two sets of doublets, one at BEs of around 707.54 and 721.06 eV, which are assigned to $2p_{3/2}$ and $2p_{1/2}$ of Fe^{2+}, respectively, and the other pair at BEs of around 713.34 and 726.16 eV corresponds to partial oxidation of Fe^{2+} to Fe^{3+} ions in $Fe(CN)_6$ fragments. The high-resolution Co 2p spectrum for STO/PB reveals two main broad peaks corresponding to $2p_{1/2}$ and $2p_{3/2}$ and their satellites. Two dominant peaks located at 781.19 and 796.67 eV are related to the +2 oxidation state of Co, Co^{2+}, and another doublet at 784.25 and 799.46 eV corresponds to the Co^{3+} cation in the PB structure, indicating the coexisting Co^{2+} and Co^{3+} cations in the PB structure of the sample.

Figure S3 depicts the XPS spectra of STO, bSTO, and bSTO/PB catalysts, complemented by atomic proportion insights extracted from XPS spectra of Sr 3d, Ti 2p, O 1s, Co 2p, and Fe 2p across all samples, as detailed in Table S1. Among the samples, STO displays the lowest atomic proportion of surface oxygen vacancies (O_v), at 1.95%. Intriguingly, the STO/PB sample demonstrates the highest atomic proportion of O_v on its surface, reaching 6.72 atm.%. Similarly, bSTO showcases a proportion of approximately 5.72%. Notably, the bSTO/PB sample reveals a lower atomic proportion of the O_v than the STO/PB sample, registering at 2.33%. This pattern is also reflected in the atomic proportion of Ti^{3+} within the samples. Specifically, STO/PB and bSTO exhibit higher atomic proportions of Ti^{3+}, approximately 4.20% and 5.34%, respectively. Conversely, STO and bSTO/PB display lower atomic proportions of Ti^{3+}, around 2.40% and 3.38%, respectively.

2.2. Photocatalytic Studies

The UV−vis diffuse reflectance spectroscopy was employed to investigate the optical characteristics of the STO, bSTO, STO/PB, and bSTO/PB samples (Figure 4a). In STO and bSTO, the distinctive absorption band extends up to 400 nm, corresponding to the electronic transition between the O 2p orbitals in the valence band and the Ti 2p orbitals in the conduction band. Conversely, the STO/PB and bSTO/PB samples reveal a broad absorption across the 400−750 nm range due to the electronic interaction between the STO and PB particles. This broad absorption phenomenon within the visible range, with greater intensity in the case of STO/PB compared to bSTO/PB, signifies the distinctive charge transfer present in CoFe-PB structures. This finding provides evidence that the core−shell system demonstrates activity within the visible spectrum.

The photocatalytic water oxidation performance of STO, bSTO, STO/PB, and bSTO/PB samples was evaluated under solar irradiation with the addition of 5 mM $Na_2S_2O_8$ as a sacrificial agent (Figure 4b). For comparison, the water oxidation activity of persulfate was also included. The STO/PB core−shell assembly exhibits an enhanced oxygen evolution activity of 129.6 μmol g^{-1} h^{-1} during a 3-h photocatalytic experiment, which is ca. 2.2 times higher than that of bare STO (57.7 μmol g^{-1} h^{-1}). Moreover, the similar performance of STO/PB in 3 consequence cycles reveals that the hybrid assembly maintains its activity and stability over a 9 h photocatalytic experiment. Throughout all cycles, there was a decline in activity after the first hour, which could be due to the consumption of the electron scavenger. This enhancement could be assigned to a more effective charge separation and transfer ability of the STO/PB sample compared to the bare STO. In a similar study involving the MnO_x/CdS/Ti^{3+}-$SrTiO_3$ core−shell heterojunction, the MnO_x/CdS/Ti^{3+}-$SrTiO_3$ structure exhibited an OER performance of approximately ∼290 μmol/g·h after 3 h, whereas the CdS/Ti^{3+}-$SrTiO_3$ and MnO_x/Ti^{3+}-$SrTiO_3$ demonstrated performances of approximately ∼60 and ∼50 μmol/g·h, respectively.[43]

On the other hand, bSTO exhibits a higher oxygen generation rate (76.3 μmol g^{-1} h^{-1}) than STO, likely attributed to its increased oxygen defects and reduced bandgap. However, introducing a PB layer on bSTO (bSTO/PB) diminishes the oxygen evolution activity to a level close to that of STO (50.7 μmol g^{-1} h^{-1}). Evidently, pairing bSTO with PB leads to a significant reduction in the oxygen evolution activity, suggesting a poor energy alignment between bSTO and PB through charge carriers.

Photocatalytic experiments with a 420 nm cutoff filter were also conducted to elucidate the light-harvesting capacities activity of STO, bSTO, and STO/PB in the visible region (Figure S4). The bSTO sample exhibits the highest water oxidation activity of 41.8 μmol g^{-1} h^{-1} due to increased oxygen defects on the $SrTiO_3$ surface, significantly enhancing the light absorption in the visible region (as from Figure 4a, nearly 90% absorbance at 800 nm). Notably, while STO is almost inactive when exposed to visible light, the STO/PB sample generates oxygen with a 34.4 μmol g^{-1} h^{-1} rate, which is remarkably lower than the "no filter" case. Thus, CoFe-PB serves not only as a water oxidation catalyst but also as a visible light harvester in the core−shell assembly.

The Mott−Schottky plots were generated for the STO, bSTO, STO/PB, and bSTO/PB samples, as depicted in Figure 4c and Figure S5. The determination of the flat band position in these samples followed this equation:

$$\frac{1}{C^2} = \frac{2}{\varepsilon_0 \varepsilon_r e N_D}\left[V - V_{FB} - \frac{k_B T}{e}\right] \quad (1)$$

Here, C represents the interfacial capacitance, ε_0 denotes the vacuum permittivity, ε_r signifies the semiconductor's dielectric constant, N_D indicates the carrier density, V corresponds to the applied voltage, k_B is the Boltzmann constant, T stands for the absolute temperature, and e symbolizes the electronic charge. The point where the linear segment of the $1/C^2$ versus applied potential (V) curve intersects the horizontal axis is indicative of V_{FB}. The positively inclined slope observed in the STO electrode (Figure S5a) confirms its n-type semiconductor nature. The flat band potential of STO was estimated at −0.66 V (vs NHE), consistent with a previous study.[43] This aligns with the common

https://doi.org/10.1021/acsmaterialsau.3c00090
ACS Mater. Au 2024, 4, 214−223

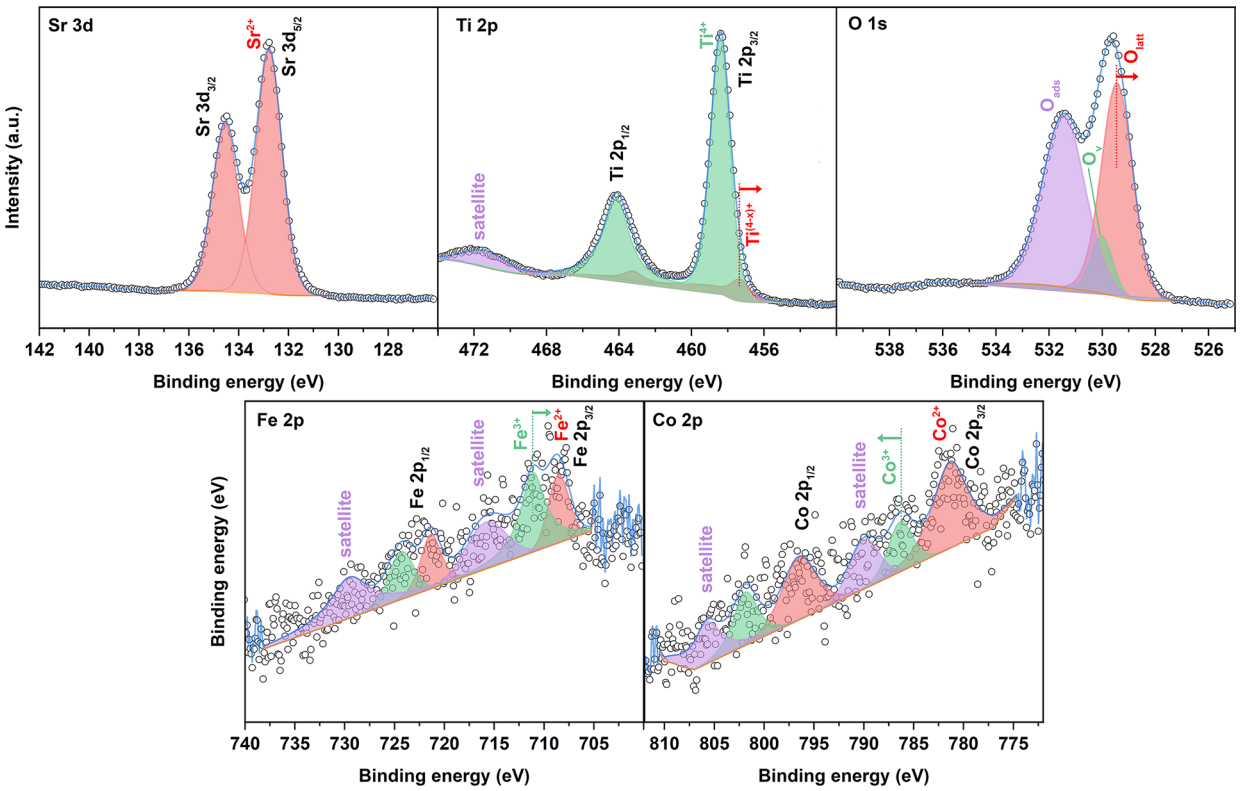

Figure 5. High-resolution XPS spectra of Sr 3d, Ti 2p, O 1s, Co 2p, and Fe 2p for the STO/PB catalyst after 3 consequent cycles of photocatalytic water oxidation.

assumption that the conduction band edge potential of an n-type metal oxide semiconductor is around 0.1−0.4 eV more negative compared to the flat band potential. This value is traditionally considered to be 0.4 eV for STO[45] resulting in a conduction band edge of −1.06 V (vs NHE). Figure 4c demonstrates that the flat band potential of STO/PB shifts toward more positive values, indicating reduced bending of STO band edges upon coupling with PB. Conversely, the p-type semiconducting character of the PB structure is discerned from the Mott−Schottky analysis of the core−shell material and corroborates previous research.[37] The distinctive reverse V-shaped Mott−Schottky plot observed for the STO/PB system is compelling evidence of p−n junction formation. This phenomenon lucidly explains the heightened photocurrent and improved photocatalytic water oxidation activity observed in the STO/PB sample. The p−n junction formation generates a potent electric field within the space charge region and concurrently decreases the charge transfer resistance at the interface. This synergistically enhances the dynamics of charge carriers at the electrode/electrolyte interface. Further examination of Figure S5b and c reveals that bSTO demonstrates a flat band potential of −0.65 V. Interestingly, there is only marginal change observed in the flat band potential of bSTO/PB, which remains steady at −0.64 V. Additionally, akin to the STO/PB case, a V-shaped Mott−Schottky plot is evident for bSTO/PB.

Finally, a cyclic voltammetry measurement reveals the HOMO level of the PB structure in STO/PB and bSTO/PB samples to be around 1.62 V vs NHE (Figure 4d and Figure S6c).

2.3. Post-photocatalysis Characterization

To assess the changes in the photocatalysts following multiple cycles of photocatalytic water oxidation, post-XPS characterizations were conducted, the results of which are depicted in Figure 5 and Figure S7. In Figure 5, the high-resolution XPS spectra of the STO/PB sample reveal the continued presence of both Co and Fe shell elements, signifying the photostability of the shell. Interestingly, while the binding energies of Sr remained unchanged, $Ti^{(4-x)+}$ shifted to lower binding energies compared with the initial sample (from 458.68 to 457.35 eV). Furthermore, the Co 2p XPS core spectrum showed that Co^{3+} shifted to higher binding energies (from 784.25 to 786.29 eV). Given that the valence band value in STO samples is primarily influenced by the O 1s state and the conduction band is governed by the Ti 3d state, the lower binding energies of $Ti^{(4-x)+}$ indicate a higher electron density in the Ti 3d state, while the higher binding energies of Co^{3+} suggest a lower electron density in the shell. This indicates that charges flow from the PBA shell to the conduction band of the STO core. Conversely, the O 1s states shifted to lower binding energies, signifying a higher electron density. This shift implies that holes migrate from the core valence band to the shell. What is more, the Fe 2p XPS core spectrum revealed a shift of Fe^{3+} to lower binding energies (from 713.34 to 711.21 eV), suggesting an increased electron density. This observation likely indicates an electron flow between Fe and Co within the PB shell. It is worth noting that the same trend is observed for the bSTO/PB sample (refer to Figure S7).

FTIR spectra were also studied for pristine and postcatalytic powder samples of STO, bSTO, and STO/PB (Figure S8). STO and STO/PB were observed to be stable during the photocatalytic water oxidation process based on comparing the FTIR profiles of pristine and postcatalytic samples. bSTO, however, exhibits additional peaks in the postcatalytic sample, which could be attributed to the adsorption of phosphate and water

https://doi.org/10.1021/acsmaterialsau.3c00090
ACS Mater. Au 2024, 4, 214−223

molecules on the surface of bSTO under photocatalytic conditions.

2.4. Proposed Mechanism

Since the core−shell structure should have a proper band energy alignment for efficient hole transfer from the STO core to the PB shell during the water oxidation, the VB position was further analyzed through VB XPS spectra of the samples seen in Figure S9. In the VB XPS analysis of STO, the top of the valence band is positioned at 1.93 and 1.71 eV. However, the VB XPS top is at 1.90 and 1.34 eV for STO/PB. Notably, the VB of STO/PB experiences a shift of 0.03 eV and forms a tail up reaching up to 1.74 eV (the VB is approximately 0.4 eV higher than the VB XPS). Turning to bSTO, its VB XPS registers a VB top at 2.07 and 1.40 eV, while they are 1.83 and 1.50 eV for bSTO/PB. Analyzing the upward tail-up values in the VB tails of bSTO and bSTO/PB, it can be deduced that the peak of the VB tail for these samples is positioned at 1.80 and 1.90 eV, respectively.

From the outcomes, it can be concluded that the valence band of the samples is at a more positive potential, in comparison to that of PB (1.62 V). Therefore, the core−shell assembly exhibits a proper band energy alignment for efficient hole transfer from the samples to the PB structure during water oxidation. Of particular note is that the upward extensions in the valence band tails for STO/PB and bSTO (1.74 and 1.80 eV) align more closely with that of PB (1.62 V) compared to bSTO/PB and STO. This observation supports the enhanced water oxidation activity in the former set of samples in contrast to the latter.

Based on the results obtained from the XPS valence band and Mott−Schottky analyses, a schematic energy band diagram (Figure 6) was constructed to provide a clearer understanding of

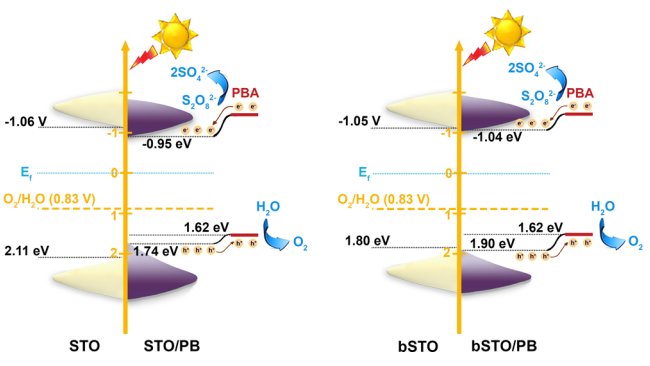

Figure 6. Schematic energy band diagram of STO, STO/PB, bSTO, and bSTO/PB samples.

the energy levels. For added insight, the bandgaps of the samples were determined utilizing DRS techniques, as illustrated in Figure S10. Comprehending the dynamics of photocatalytic water splitting relies heavily on this energy band model, as it serves as the framework for critical processes including charge generation, separation, and transfer when exposed to light. A precise prediction of the positions of the VB, CB, HOMO, and LUMO levels within the system components is pivotal for interpreting the outcomes of photocatalytic water splitting.

As shown in Figure 6, the photocatalytic process commences with the absorption of light by STO/PB, leading to the generation of electrons and holes. The holes located within the VB of STO/PB are subsequently transferred to the HOMO level of CoFe-PB, strategically positioned between the VB of STO and the water oxidation level. Consequently, these holes play a pivotal role in driving the water oxidation process. Utilizing the insights gained from the post-XPS findings (Figure 5), it is evident that charges flow from the PBA shell to the conduction band of the STO core. Conversely, holes migrate from the core valence band to the shell, establishing a crucial charge transfer mechanism within this innovative core−shell assembly.

While there is not a significant disparity in the conduction band position among the samples, a noticeable downward shift in the conduction band for STO/PB is evident, transitioning from −1.06 to −0.95 V. On the other hand, it could be seen that the VB edge of STO/PB turns to be broad at an enhanced oxygen vacancy concentration. Meanwhile, the band of defect states resulting from oxygen vacancies is very close to the HOMO level of PB, allowing photogenerated electrons to easily exchange between two bands, the main reason for the enhanced catalytic activity of the STO/PB sample.

3. CONCLUSIONS

In summary, we display the development of an innovative semiconductor-catalyst core−shell architecture meticulously designed to significantly boost photocatalytic water oxidation activity. This advancement was achieved by depositing CoFe PBA particles onto both STO and bSTO nanocubes via an in situ synthetic method, establishing a well-verified core−shell structure, as demonstrated with HRTEM. The STO/PB assembly exhibits a robust p−n junction, verified by Mott−Schottky analysis. The STO/PB core−shell assembly demonstrates an oxygen evolution rate of 129.6 μmol g^{-1} h^{-1}, approximately 2.2 times greater than that of the bare STO (57.7 μmol g^{-1} h^{-1}). Furthermore, the consistent performance of STO/PB over three consecutive cycles illustrates that this hybrid assembly retains its activity and stability throughout a 9 h photocatalytic experiment. This enhancement in performance can be attributed to the properly aligned band energy position of the STO/PB p−n junction assembly compared to that of bare STO, which facilitates efficient hole transfer from the STO to the PB structure during the water oxidation process. Conversely, bSTO demonstrates a higher oxygen generation rate (76.3 μmol g^{-1} h^{-1}) than STO does, attributed to increased oxygen defects and a reduced bandgap. However, the introduction of a PB layer on bSTO (bSTO/PB) markedly reduced the oxygen evolution activity, falling even below that of STO (50.7 μmol g^{-1} h^{-1}). These outcomes underscore the potential of tailored semiconductor-catalyst interfaces in advancing the field of photocatalysis, highlighting their pivotal role in driving sustainable water oxidation processes.

4. EXPERIMENTAL SECTION

4.1. Chemicals and Reagents

All chemicals were used as obtained without any further purification. Strontium nitrate ($Sr(NO_3)_2$, Sigma-Aldrich, > 99.9%), titanium(IV) butoxide ($Ti(OCH_2CH_2CH_2CH_3)_4$, Sigma-Aldrich, >98.0%), nitric acid (HNO_3, Merck, 65%), ethanol (CH_3CH_2OH, ISOLAB, >99.9%), potassium hexacyanoferrate ($K_3[Fe(CN)_6]$, Sigma-Aldrich, 99.0%), cobalt(II) nitrate hexahydrate ($Co(NO_3)_2{\cdot}6H_2O$, Alfa Aesar, 99.9%), sodium borohydride ($NaBH_4$, ReagentPlus, 99%) is used in all experiments.

4.2. Preparation of $SrTiO_3$ (STO)

STO powder was prepared from $Sr(NO_3)_2$ and $Ti(OCH_2CH_2CH_2CH_3)_4$ via a hydrothermal method. In a typical synthesis, 3.7 mL of $Ti(OCH_2CH_2CH_2CH_3)_4$ was added to 50 mL of ethanol, and 2.3 g of $Sr(NO_3)_2$ was dissolved in 20 mL of water. After 30 min of stirring at room temperature, the $Sr(NO_3)_2$ solution was quickly added to the $Ti(OCH_2CH_2CH_2CH_3)_4$-containing solution,

https://doi.org/10.1021/acsmaterialsau.3c00090
ACS Mater. Au 2024, 4, 214−223

and the mixture was stirred for another 30 min. Then, the mixed solution was transferred to a 100 mL Teflon-lined autoclave and heated at 180 °C for 24 h. The white precipitate was collected by vacuum filtration, washed with ethanol and water, and dried at 70 °C for 2 h. The obtained powder was leached with 0.5 M HNO_3 to remove $SrCO_3$ impurities, rinsed with ethanol and deionized water, and left for drying in an oven overnight.

4.3. Preparation of Blue $SrTiO_3$ (bSTO)

As previously detailed, the synthesis of bSTO powder was accomplished via a solid-state reaction involving $NaBH_4$ and crystalline STO.[46] To elaborate briefly, 25 mmol of STO powder was combined with 25 mmol of $NaBH_4$ and ground together in an agate mortar. This mixture was subsequently placed in a porcelain boat and subjected to heating in a tube furnace under an Ar^+/H_2 atmosphere. The temperature was gradually increased to 450 °C at a rate of 10 °C per minute, and the material was held at this temperature for 1 h before being allowed to cool to room temperature. The resulting powder was then subjected to several washes with water and ethanol to eliminate residual $NaBH_4$, followed by drying at 80 °C.

4.4. Preparation of PB-Coated STO and bSTO (STO/PB and bSTO/PB)

An in situ synthetic procedure was adopted for the preparation of hybrid assemblies. Typically, 0.2725 mmol of $K_3[Fe(CN)_6]$ was dissolved in 10 mL of water, added dropwise to a previously sonicated STO powder solution (50 mg of STO in 10 mL of water) at room temperature, and stirred for 21 h. The STO/$Fe(CN)_6$ precipitate was collected by centrifugation and rinsed 3 times with water. The obtained solid was dispersed in deionized water and sonicated again. Then, aqueous $Co(NO_3)_2{\cdot}6H_2O$ (0.4087 mmol in 10 mL of water) was added dropwise to the above solution, and the mixture was stirred for 21 h. This procedure is repeated twice to improve coating efficiency. The final precipitate was separated by centrifugation, washed 3 times with water, and dried at 70 °C. The bSTO/PB hybrid structure was synthesized using an analogous approach.

4.5. Electrochemical Measurements

Mott−Schottky measurements were conducted using an AutoLab Potentiostat Galvanostat (PGSTAT302N, The Netherlands) within a standard three-electrode system immersed in a 0.1 M Na_2SO_4 solution. A reversible hydrogen electrode (RHE; HydroFlex) was employed as the reference electrode, while a Pt spring served as the counter electrode. The FTO glasses were meticulously cleaned through sonication with water, followed by ethanol and acetone. A solution containing 20 μL of Nafion dispersed in 5 mL of ethanol−water solution was prepared, and 2 mg of each sample was dispersed within this solution. Sonication was applied for an hour to ensure uniform distribution of the sample. Subsequently, 50 μL of the prepared ink solution was deposited onto the FTO surface and left to air-dry at room temperature. Mott−Schottky measurements were initiated at an initial potential of −0.8 V, progressing to a final potential of 0 V with an increment of 0.1 V. These measurements were recorded at a frequency of 5 kHz.

4.6. Photocatalytic O_2 Evolution

The photocatalytic experiments for oxygen evolution were carried out in a 16.5 mL Pyrex reactor at room temperature. Typically, 5 mg of the catalyst was dispersed in 10 mL of deionized water containing 5 mM $Na_2S_2O_8$ as a sacrificial agent. The reaction solution was deaerated by bubbling N_2 gas for 30 min before light irradiation. The reactor was sealed by using two rubber septa, and the gap between them was purged with N_2 to prevent a possible O_2 leak during the measurements. A Xe lamp (300 W; AM 1.5 global filter) was used as a light source. A 420 nm long-pass filter was employed for experiments conducted under visible light irradiation. The amount of generated O_2 was measured by introducing 100 μL of the reactor headspace gas into a gas chromatograph (Agilent 7820A GC, with molecular sieve column and a TCD detector). Ar was used as the carrier gas.

4.7. Characterization

X-ray diffraction (XRD) patterns of samples were obtained on a Rigaku Miniflex diffractometer equipped with a Cu Kα (λ= 1.54056 Å) X-ray source, operating at 30 kV 15^{-1} and a Scintillator NaI(T1) detector with a Be window. The diffraction patterns were recorded within the 10−80° range with a scan step of 0.04. Fourier transform infrared (FT-IR) spectra were recorded with a Bruker Alpha Platinum-ATR spectrometer with 4 cm^{-1} resolution in a wavenumber range between 4000 and 400 cm^{-1}. The morphology was examined using a field-emission scanning electron microscope (FE-SEM) model Zeiss Ultra Plus. Further investigation of the microstructure involved high-resolution transmission electron microscopy (HRTEM; Hitachi HF5000 200 kV (S)TEM, operated in HR mode) to analyze lattice fringes, selected area electron diffraction (SAED), high-angle annular dark-field scanning transmission electron microscopy (HAADF-STEM) images, and accompanying EDS-STEM mappings. Surface composition and oxidation states were determined through X-ray photoelectron spectroscopy (XPS) using a Thermo Scientific K-Alpha instrument equipped with an Al Kα monochromator source (1486.6 eV). All XPS spectra were adjusted based on the binding energy of C 1s at 284.50 eV. The optical band gaps of the photocatalysts in their as-prepared state were measured using a SHIMADZU UV-3600 UV−vis-NIR spectrophotometer in the reflectance mood. UV−vis absorption spectra were collected over the ultraviolet to visible range, specifically from 220 to 800 nm.

■ ASSOCIATED CONTENT

Supporting Information

The Supporting Information is available free of charge at https://pubs.acs.org/doi/10.1021/acsmaterialsau.3c00090.

Additional SEM and HRTEM images, XPS results, photocatalytic oxygen evolution activities in the visible region, Mott−Schottky, Kubelka−Munk, CV plots, as well as XPS valence band and ATR-FTIR spectra (PDF)

■ AUTHOR INFORMATION

Corresponding Authors

Umut Aydemir − *Koç University Boron and Advanced Materials Application and Research Center (KUBAM), Sariyer, Istanbul 34450, Türkiye; Department of Chemistry, Koç University, Sariyer, Istanbul 34450, Türkiye;* orcid.org/0000-0003-1164-1973; Email: uaydemir@ku.edu.tr

Ferdi Karadas − *Department of Chemistry, Faculty of Science, Bilkent University, Ankara 06800, Türkiye*; Email: karadas@fen.bilkent.edu.tr

Authors

Naeimeh Sadat Peighambardoust − *Koç University Boron and Advanced Materials Application and Research Center (KUBAM), Sariyer, Istanbul 34450, Türkiye;* orcid.org/0000-0002-2991-5488

Sina Sadigh Akbari − *Department of Chemistry, Faculty of Science, Bilkent University, Ankara 06800, Türkiye*

Rana Lomlu − *Department of Chemistry, Faculty of Science, Bilkent University, Ankara 06800, Türkiye*

Complete contact information is available at: https://pubs.acs.org/10.1021/acsmaterialsau.3c00090

Author Contributions

N. S. Peighambardoust synthesized the core materials. She then performed the chemical characterizations and electrochemical experiments and their interpretation. S. Sadigh Akbari and R.

https://doi.org/10.1021/acsmaterialsau.3c00090
ACS Mater. Au 2024, 4, 214−223

Lomlu synthesized core−shell structures and performed photochemical characterizations and their interpretation. U. Aydemir and F. Karadas supervised the whole project, from synthesis to interpretation of the results. CRediT: **Naeimeh Sadat Peighambardoust** conceptualization, data curation, formal analysis, investigation, methodology, validation, writing-original draft, writing-review & editing; **Sina Sadigh Akbari** conceptualization, data curation, formal analysis, investigation, methodology, writing-original draft; **Rana Lomlu** data curation, formal analysis, investigation; **Umut Aydemir** conceptualization, funding acquisition, project administration, supervision, writing-original draft, writing-review & editing; **Ferdi Karadaş** conceptualization, funding acquisition, project administration, supervision, writing-original draft, writing-review & editing.

Notes

The authors declare no competing financial interest.

■ ACKNOWLEDGMENTS

The authors thank Dr. Barış Yağcı at Koç University Surface Science and Technology Center (KUYTAM) for his help with characterizations. We are grateful to Dr. Gülcan Çorapçıoğlu from Koç University Nanofabrication and Nanocharacterization Center (n²STAR) as well as Dr. Hiroaki Matsumoto and Keisuke Igarashi from Hitachi High-Tech Corporation, Japan for the HR-TEM measurements.

■ REFERENCES

(1) Wang, Q.; Domen, K. Particulate Photocatalysts for Light-Driven Water Splitting: Mechanisms, Challenges, and Design Strategies. *Chem. Rev.* **2020**, *120* (2), 919−985.

(2) Takata, T.; Domen, K. Particulate Photocatalysts for Water Splitting: Recent Advances and Future Prospects. *ACS Energy Lett.* **2019**, *4* (2), 542−549.

(3) Hisatomi, T.; Kubota, J.; Domen, K. Recent Advances in Semiconductors for Photocatalytic and Photoelectrochemical Water Splitting. *Chem. Soc. Rev.* **2014**, *43* (22), 7520−7535.

(4) Avcıoğlu, C.; Avcıoğlu, S.; Bekheet, M. F.; Gurlo, A. Photocatalytic Overall Water Splitting by $SrTiO_3$: Progress Report and Design Strategies. *ACS Appl. Energy Mater.* **2023**, *6* (3), 1134−1154.

(5) Phoon, B. L.; Lai, C. W.; Juan, J. C.; Show, P. L.; Pan, G. T. Recent Developments of Strontium Titanate for Photocatalytic Water Splitting Application. *Int. J. Hydrogen Energy* **2019**, *44* (28), 14316−14340.

(6) Cheng, C.; Long, R. Charge-Compensated Doping Extends Carrier Lifetimes in $SrTiO_3$ by Passivating Oxygen Vacancy Defects. *J. Phys. Chem. Lett.* **2021**, *12* (50), 12040−12047.

(7) Konta, R.; Ishii, T.; Kato, H.; Kudo, A. Photocatalytic Activities of Noble Metal Ion Doped $SrTiO_3$ under Visible Light Irradiation. *J. Phys. Chem. B* **2004**, *108* (26), 8992−8995.

(8) Sayama, K.; Mukasa, K.; Abe, R.; Abe, Y.; Arakawa, H. Stoichiometric Water Splitting into H_2 and O_2 Using a Mixture of Two Different Photocatalysts and an IO^{3-}/I^- Shuttle Redox Mediator under Visible Light Irradiation. *Chem. Commun.* **2001**, *1* (23), 2416−2417.

(9) Sasaki, Y.; Nemoto, H.; Saito, K.; Kudo, A. Solar Water Splitting Using Powdered Photocatalysts Driven by Z-Schematic Interparticle Electron Transfer without an Electron Mediator. *J. Phys. Chem. C* **2009**, *113* (40), 17536−17542.

(10) Ham, Y.; Hisatomi, T.; Goto, Y.; Moriya, Y.; Sakata, Y.; Yamakata, A.; Kubota, J.; Domen, K. Flux-Mediated Doping of $SrTiO_3$ Photocatalysts for Efficient Overall Water Splitting. *J. Mater. Chem. A Mater.* **2016**, *4* (8), 3027−3033.

(11) Wang, Q.; Hisatomi, T.; Jia, Q.; Tokudome, H.; Zhong, M.; Wang, C.; Pan, Z.; Takata, T.; Nakabayashi, M.; Shibata, N.; Li, Y.; Sharp, I. D.; Kudo, A.; Yamada, T.; Domen, K. Scalable Water Splitting on Particulate Photocatalyst Sheets with a Solar-to-Hydrogen Energy Conversion Efficiency Exceeding 1%. *Nat. Mater.* **2016**, *15* (6), 611−615.

(12) Chiang, T. H.; Lyu, H.; Hisatomi, T.; Goto, Y.; Takata, T.; Katayama, M.; Minegishi, T.; Domen, K. Efficient Photocatalytic Water Splitting Using Al-Doped $SrTiO_3$ Coloaded with Molybdenum Oxide and Rhodium-Chromium Oxide. *ACS Catal.* **2018**, *8* (4), 2782−2788.

(13) Wang, G.; Ling, Y.; Li, Y. Oxygen-Deficient Metal Oxide Nanostructures for Photoelectrochemical Water Oxidation and Other Applications. *Nanoscale* **2012**, *4* (21), 6682−6691.

(14) Liu, N.; Schneider, C.; Freitag, D.; Hartmann, M.; Venkatesan, U.; Muller, J.; Spiecker, E.; Schmuki, P. Black TiO_2 Nanotubes: Cocatalyst-Free Open-Circuit Hydrogen Generation. *Nano Lett.* **2014**, *14*, 3309−3313.

(15) Bai, X.; Wang, L.; Zong, R.; Lv, Y.; Sun, Y.; Zhu, Y. Performance Enhancement of ZnO Photocatalyst via Synergic Effect of Surface Oxygen Defect and Graphene Hybridization. *Langmuir* **2013**, *29* (9), 3097−3105.

(16) Lv, Y.; Zhu, Y.; Zhu, Y. Enhanced Photocatalytic Performance for the $BiPO_{4-x}$ Nanorod Induced by Surface Oxygen Vacancy. *J. Phys. Chem. C* **2013**, *117* (36), 18520−18528.

(17) Kong, M.; Li, Y.; Chen, X.; Tian, T.; Fang, P.; Zheng, F.; Zhao, X. Tuning the Relative Concentration Ratio of Bulk Defects to Surface Defects in TiO_2 Nanocrystals Leads to High Photocatalytic Efficiency. *J. Am. Chem. Soc.* **2011**, *133* (41), 16414−16417.

(18) Sun, D.; Zhang, Y.; Yan, S.; Sun, K.; Wang, G.; Bu, Y.; Xie, G. Fabrication of Excellent Heterojunction Assisting by Interfaced Oxygen Vacancy to Improve the Separation Capacity of Photogenerated Carriers. *Adv. Mater. Interfaces* **2018**, *5* (5), 1−9.

(19) Tan, H.; Zhao, Z.; Zhu, W.-b.; Coker, E. N.; Li, B.; Zheng, M.; Yu, W.; Fan, H.; Sun, Z. Oxygen Vacancy Enhanced Photocatalytic Activity of Pervoskite $SrTiO_3$. *ACS Appl. Mater. Interfaces* **2014**, *6* (21), 19184−19190.

(20) Mu, L.; Zhao, Y.; Li, A.; Wang, S.; Wang, Z.; Yang, J.; Wang, Y.; Liu, T.; Chen, R.; Zhu, J.; Fan, F.; Li, R.; Li, C. Enhancing Charge Separation on High Symmetry $SrTiO_3$ Exposed with Anisotropic Facets for Photocatalytic Water Splitting. *Energy Environ. Sci.* **2016**, *9* (7), 2463−2469.

(21) Sasaki, Y.; Iwase, A.; Kato, H.; Kudo, A. The Effect of Co-Catalyst for Z-Scheme Photocatalysis Systems with an Fe^{3+}/Fe^{2+} Electron Mediator on Overall Water Splitting under Visible Light Irradiation. *J. Catal.* **2008**, *259* (1), 133−137.

(22) Qureshi, M.; Garcia-Esparza, A. T.; Jeantelot, G.; Ould-Chikh, S.; Aguilar-Tapia, A.; Hazemann, J. L.; Basset, J. M.; Loffreda, D.; Le Bahers, T.; Takanabe, K. Catalytic Consequences of Ultrafine Pt Clusters Supported on $SrTiO_3$ for Photocatalytic Overall Water Splitting. *J. Catal.* **2019**, *376*, 180−190.

(23) Lyu, H.; Hisatomi, T.; Goto, Y.; Yoshida, M.; Higashi, T.; Katayama, M.; Takata, T.; Minegishi, T.; Nishiyama, H.; Yamada, T.; Sakata, Y.; Asakura, K.; Domen, K. An Al-Doped $SrTiO_3$ Photocatalyst Maintaining Sunlight-Driven Overall Water Splitting Activity for over 1000 h of Constant Illumination. *Chem. Sci.* **2019**, *10* (11), 3196−3201.

(24) Zhou, D.; Wang, G.; Feng, Y.; Chen, W.; Chen, J.; Yu, Z.; Zhang, Y.; Wang, J.; Tang, L. CuS Co-Catalyst Modified Hydrogenated $SrTiO_3$ nanoparticles as an Efficient Photocatalyst for H_2 evolution. *Dalton Transactions* **2021**, *50* (22), 7768−7775.

(25) Takata, T.; Jiang, J.; Sakata, Y.; Nakabayashi, M.; Shibata, N.; Nandal, V.; Seki, K.; Hisatomi, T.; Domen, K. Photocatalytic Water Splitting with a Quantum Efficiency of Almost Unity. *Nature* **2020**, *581* (7809), 411−414.

(26) Hegner, F. S.; Galán-Mascarós, J. R.; López, N. A Database of the Structural and Electronic Properties of Prussian Blue, Prussian White, and Berlin Green Compounds through Density Functional Theory. *Inorg. Chem.* **2016**, *55* (24), 12851−12862.

(27) Pintado, S.; Goberna-Ferrón, S.; Escudero-Adán, E. C.; Galán-Mascarós, J. R. Fast and Persistent Electrocatalytic Water Oxidation by Co-Fe Prussian Blue Coordination Polymers. *J. Am. Chem. Soc.* **2013**, *135* (36), 13270−13273.

(28) Goberna-Ferron, S.; Hernandez, W. Y.; Rodriguez-Garcia, B.; Galan-Mascaros, J. R. Light-Driven Water Oxidation with Metal

https://doi.org/10.1021/acsmaterialsau.3c00090
ACS Mater. Au 2024, 4, 214−223

Hexacyanometallate Heterogeneous Catalysts. *ACS Catal.* **2014**, *4* (6), 1637−1641.
(29) Ahmad, A. A.; Ulusoy Ghobadi, T. G.; Buyuktemiz, M.; Ozbay, E.; Dede, Y.; Karadas, F. Light-Driven Water Oxidation with Ligand-Engineered Prussian Blue Analogues. *Inorg. Chem.* **2022**, *61* (9), 3931.
(30) Ulusoy Ghobadi, T. G.; Ozbay, E.; Karadas, F. How to Build Prussian Blue Based Water Oxidation Catalytic Assemblies: Common Trends and Strategies. *Chem.—Eur. J.* **2021**, *27* (11), 3638−3649.
(31) Han, L.; Tang, P.; Reyes-Carmona, Á.; Rodríguez-García, B.; Torréns, M.; Morante, J. R.; Arbiol, J.; Galan-Mascaros, J. R. Enhanced Activity and Acid PH Stability of Prussian Blue-Type Oxygen Evolution Electrocatalysts Processed by Chemical Etching. *J. Am. Chem. Soc.* **2016**, *138* (49), 16037−16045.
(32) Yamada, Y.; Oyama, K.; Gates, R.; Fukuzumi, S. High Catalytic Activity of Heteropolynuclear Cyanide Complexes Containing Cobalt and Platinum Ions: Visible-Light Driven Water Oxidation. *Angewandte Chem. International Edition* **2015**, *54* (19), 5613−5617.
(33) Aratani, Y.; Oyama, K.; Suenobu, T.; Yamada, Y.; Fukuzumi, S. Photocatalytic Hydroxylation of Benzene by Dioxygen to Phenol with a Cyano-Bridged Complex Containing FeII and RuII Incorporated in Mesoporous Silica-Alumina. *Inorg. Chem.* **2016**, *55* (12), 5780−5786.
(34) Hegner, F. S.; Herraiz-Cardona, I.; Cardenas-Morcoso, D.; López, N.; Galán-Mascarós, J. R.; Gimenez, S. Cobalt Hexacyanoferrate on $BiVO_4$ Photoanodes for Robust Water Splitting. *ACS Appl. Mater. Interfaces* **2017**, *9* (43), 37671−37681.
(35) Yamada, Y.; Oyama, K.; Suenobu, T.; Fukuzumi, S. Photocatalytic Water Oxidation by Persulphate with a Ca^{2+} Ion-Incorporated Polymeric Cobalt Cyanide Complex Affording O_2 with 200% Quantum Efficiency. *Chem. Commun.* **2017**, *53* (24), 3418−3421.
(36) Akbari, S. S.; Karadas, F. Precious Metal-Free Photocatalytic Water Oxidation by a Layered Double Hydroxide-Prussian Blue Analogue Hybrid Assembly. *ChemSusChem* **2021**, *14* (2), 679−685.
(37) Akbari, S. S.; Unal, U.; Karadas, F. Photocatalytic Water Oxidation with a CoFe Prussian Blue Analogue−Layered Niobate Hybrid Material. *ACS Appl. Energy Mater.* **2021**, *4* (11), 12383−12390.
(38) Gundogdu, G.; Ulusoy Ghobadi, T. G.; Sadigh Akbari, S.; Ozbay, E.; Karadas, F. Photocatalytic Water Oxidation with a Prussian Blue Modified Brown TiO_2. *Chem. Commun.* **2021**, *57* (4), 508−511.
(39) Usman, E.; Barzgar Vishlaghi, M.; Sadigh Akbari, S.; Karadaş, F.; Kaya, S. Hybrid CuFe-CoFe Prussian Blue Catalysts on $BiVO_4$ for Enhanced Charge Separation and Injection for Photoelectrochemical Water Oxidation. *ACS Appl. Energy Mater.* **2022**, *5* (12), 15434−15441.
(40) Ulusoy Ghobadi, T. G.; Ghobadi, A.; Soydan, M. C.; Barzgar Vishlaghi, M.; Kaya, S.; Karadas, F.; Ozbay, E. Strong Light-matter Interaction in Au Plasmonic Nanoantennas Coupled with Prussian Blue Catalyst on $BiVO_4$ for Photoelectrochemical Water Splitting. *ChemSusChem* **2020**, *13*, 2577−2588.
(41) Sato, O.; Iyoda, T.; Fujishima, A.; Hashimoto, K. Photoinduced Magnetization of a Cobalt-Iron Cyanide. *Science (1979)* **1996**, *272* (5262), 704−705.
(42) Lezna, R. O.; Romagnoli, R.; de Tacconi, N. R.; Rajeshwar, K. Cobalt Hexacyanoferrate: Compound Stoichiometry, Infrared Spectroelectrochemistry, and Photoinduced Electron Transfer. *J. Phys. Chem. B* **2002**, *106* (14), 3612−3621.
(43) Pan, J.; Chen, Z.; Wang, P.; Wang, P.; Yu, Q.; Zhao, W.; Wang, J.; Zhu, M.; Zheng, Y.; Li, C. The Overall Water Splitting of CdS/Ti^{3+}-$SrTiO_3$ Core−Shell Heterojunction via OER Enhancement of MnO_x Nanoparticles. *Chemical Engineering Journal* **2021**, *424* (February), 130357.
(44) Fan, Y.; Liu, Y.; Cui, H.; Wang, W.; Shang, Q.; Shi, X.; Cui, G.; Tang, B. Photocatalytic Overall Water Splitting by $SrTiO_3$ with Surface Oxygen Vacancies. *Nanomaterials* **2020**, *10* (12), 2572.
(45) Matsumoto, Y. Energy Positions of Oxide Semiconductors and Photocatalysis with Iron Complex Oxides. *J. Solid State Chem.* **1996**, *126* (2), 227−234.
(46) Peighambardoust, N. S.; Aydemir, U. Electrophoretic Deposition and Characterization of Self-Doped $SrTiO_3$ Thin Films. *Turk J. Chem.* **2021**, *45* (2), 323−332.

https://doi.org/10.1021/acsmaterialsau.3c00090
ACS Mater. Au 2024, 4, 214−223